

## Chapter 5

# The Tomographic Imaging Camera

### 5.1 Introduction

So far in our discussion of 3-D imaging we have focused on the retrieval of depth information from a single location in the transverse plane. One way to acquire a full 3-D data set is through mechanical raster-scanning of the laser beam across the object space. The acquisition time in such systems is ultimately limited by the scan speed, and for very high resolution datasets ( $> 1$  transverse mega pixel) is prohibitively slow.

Rapid 3-D imaging is of crucial importance in *in vivo* biomedical diagnostics [21, 26] because it reduces artifacts introduced by patient motion. In addition, a high-throughput, non-destructive 3-D imaging technology is necessary to meet the requirements of several new industrial developments. The emerging fields of 3-D printing and manufacturing [27] will require high-precision and cost-effective 3-D imaging capabilities. Advances in 3-D tissue engineering, such as synthetic blood vessels [28], synthetic tendons [29], and synthetic bone tissue [30], require high-resolution 3-D imaging for tissue monitoring and quality control. To ensure higher physiological relevance of drug tests, the pharmaceutical industry is moving from two-dimensional (2-D) to 3-D cell cultures and tissue models, and high-throughput 3-D imaging will be used as a basic tool in the drug development process [31]. To date, no imaging technology exists that meets these industrial demands.

In this chapter we describe our development of a conceptually new, 3-D tomographic imaging camera (TomICam) that is capable of robust, large field of view,

and rapid 3-D imaging. We develop the TomICam theory and demonstrate its basic principle in a proof-of-concept experiment. We also discuss the application of compressive sensing (CS) to the TomICam platform. CS is an acquisition methodology that takes advantage of signal structure to compress and sample the information in a single step. It is of particular interest in applications involving large data sets, such as 3-D imaging, because compression reduces the volume of information that is recorded by the sensor, effectively speeding up the measurement. We use a series of numerical simulations to demonstrate a reduction in the number of measurements necessary to acquire sparse scatterer information with CS TomICam.

### 5.1.1 Current Approaches to 3-D Imaging and Their Limitations

A generic FMCW 3-D imaging system has two important components: an SFL for ranging and a technique to translate the one-pixel measurement laterally in two dimensions to capture the full 3-D scene. The basic principle of FMCW ranging is illustrated in figure 5.1. The optical frequency of a single-mode laser is varied linearly with time, with a slope  $\xi$ . The output of the laser is incident on a target sample and the reflected signal is mixed with a part of the laser output in a photodetector (PD). If the relative delay between the two light paths is  $\tau$ , the PD output is a sinusoidal current with frequency  $\xi\tau$ . The distance to the sample is determined by taking a Fourier transform of the detected photocurrent. Reflections from multiple scatterers at different depths result in separate frequencies in the photocurrent.

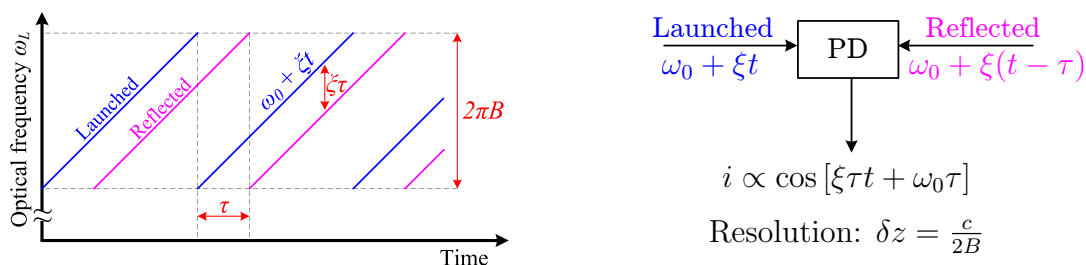


Figure 5.1: Principle of FMCW imaging with a single reflector

The important metrics of an SFL are first, the sweep linearity—a highly linear source reduces the data-processing overhead—and, second, the total frequency excursion,  $B$ , which determines the axial ( $z$ ) resolution (see figure 5.1 and equation (5.3)). State-of-the-art SFL sources for biomedical and other imaging applications are typically mechanically-tuned external-cavity lasers where a rotating grating tunes the lasing frequency [26, 48, 63]. Excursions in excess of 10 THz, corresponding to axial resolutions of about 10  $\mu\text{m}$  [26, 48] have been demonstrated for biomedical imaging applications. Fourier-domain mode locking (FDML) [64] and quasi-phase continuous tuning [65] have been developed to further improve the tuning speed and lasing properties of these sources. However, all these approaches suffer from complex mechanical embodiments that lead to a high system cost and limit the speed, linearity, coherence, size, reliability, and ease of use of the SFL.

Detectors for 3-D imaging typically rely on mechanical scanning of a single-pixel measurement across the scene [66], as shown schematically in figure 5.2a. The combination of high lateral resolution ( $< 10 \mu\text{m}$ ) and large field of view ( $> 1 \text{ cm}$ ), requires scanning over millions of pixels, resulting in slow acquisition. The mechanical nature of the beam scanning is unattractive for high-throughput, industrial applications, due to a limited speed and reliability. It is therefore desirable to eliminate the requirement for beam scanning, and obtain the information from the entire field of view in one shot. This is possible using a 2-D array of photodetectors and floodlight illumination. However, in a high-axial-resolution system, each detector in the array measures a beat signal  $\xi\tau$  in the MHz regime. A large array of high speed detectors therefore needs to operate at impractical data rates ( $\sim\text{THz}$ ) and is prohibitively expensive. For this reason, full-field FMCW imaging systems have been limited to demonstrations with extremely slow scanning rates [25, 66] or expensive small arrays [67].

A further limitation of FMCW imaging is the need to process the photodetector information. This processing typically consists of taking a Fourier transform of the photocurrent at each lateral ( $x, y$ ) position. In applications requiring real-time imaging, e.g., autonomous navigation [68], it is desirable to minimize the amount of processing overhead.

An ideal FMCW 3-D imaging system will therefore consist of a rapidly tuned SFL with a large frequency sweep and a detection technique that is capable of measuring the lateral extent of the object in one shot. The system will be inexpensive, robust, and contain no moving parts. The TomICam platform achieves these goals through its use of low-cost low-speed detector arrays. It takes advantage of the linearity and starting frequency stability of the optoelectronic SFL (see chapter 3), as well as our development of SFLs at wavelengths compatible with off-the-shelf silicon cameras (1060 nm and 850 nm). Moreover, TomICam is inherently compatible with novel compressive acquisition schemes [69], which leads to further increases in the acquisition speed.

Various other approaches to 3-D imaging have been described in literature, and recent work is summarized in table 5.1. Broadly speaking, the depth information is obtained using time-of-flight (TOF) or FMCW techniques. Transverse imaging is obtained either by mechanical scanning or using a full-field detector array. In some embodiments, compressive sensing ideas are used to reduce the number of measurements necessary to obtain the full 3-D image. TOF ranging systems illuminate the sample with a pulsed light source, and measure the arrival time of the reflected pulse(s) to obtain depth information. As a result, the axial resolution of TOF systems is limited by the pulse-width of the optical source, as well as the bandwidth of the detector. Ongoing TOF experiments rely on expensive femto/pico-second mode-locked lasers and/or acquisition systems with large bandwidths ( $\simeq 10$ s of GHz), in order to achieve sub-cm axial resolution [17]. Transverse imaging is typically achieved using mechanically scanned optics [16]. Full-field imaging systems using specially designed demodulating pixels have also been demonstrated; however, these systems have significantly lower axial resolution ( $\simeq 10$ s of cm) and a limited unambiguous depth of range [70].

FMCW ranging has many advantages over the TOF approach, since it eliminates the need for narrow optical pulses or accurate high-speed optical detectors and electronics (see chapter 2). Very high resolution systems ( $< 10 \mu\text{m}$ ) have been demonstrated, and have found many applications, e.g., swept-source optical coherence

	Technology	Axial resolution	Transverse imaging	Hardware requirement	Limitations	Compressive sensing
TOF	TOF-LIDAR [16]	$\simeq 2$ cm	Mechanical scanning	Mode-locked laser, fast electronics	Slow scanning, moving parts, expensive components, limited resolution	Not used in cited work
	Single-pixel TOF-LIDAR [17]	$\simeq 1$ cm	Spatial light modulator, single pixel detector	Mode-locked laser, fast electronics, SLM	Expensive components, limited resolution	Used to convert the single-pixel data into a 3D model
	Lock-in TOF [70]	10s of cm	Lock-in pixel CCD	Specially engineered lock-in pixel CCD	Poor resolution, limited lock-in CCD size	Not used
FMCW	SS-OCT/CS-OCT [71]	1–10 $\mu\text{m}$	Mechanical scanning	External cavity chirped laser with moving parts, slow detector	Slow scanning, moving parts, bulky and fragile	Used to reduce scan time
	TomICam	10–100 $\mu\text{m}$	CCD/CMOS array	Optoelectronic SFL (no moving parts), standard CCD/CMOS sensor	Floodlight illumination (higher power)	Reduced acquisition time and power

Table 5.1: Recent 3-D camera embodiments

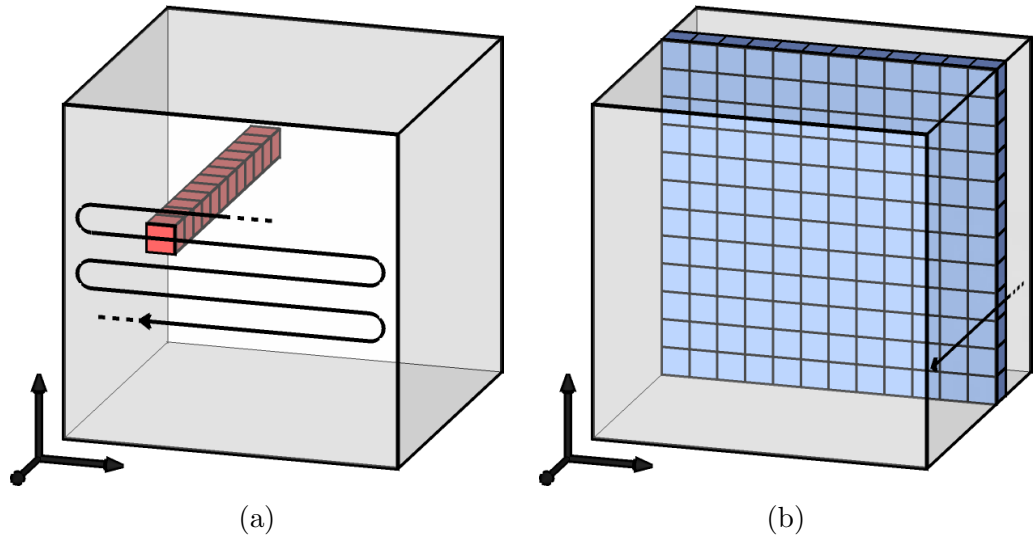


Figure 5.2: (a) Volume acquisition by a raster scan of a single-pixel FMCW measurement across the object space. (b) Volume acquisition in a TomICam system. 3-D information is recorded one transverse slice at a time. The measurement depth is chosen electronically by setting the frequency of the modulation waveform.

tomography [71].

The TomICam approach is unique, in that it combines the high resolution of FMCW ranging, along with full-field imaging using a detector array, thereby eliminating any mechanical beam scanning optics. Moreover, it does not require specially engineered detectors pixels, unlike the lock-in TOF lidar [70], making it more versatile and scalable. Specifically, state-of-the-art lock-in CCDs are limited to tens of thousands of pixels, while standard low-speed CMOS/CCD sensors with tens of mega pixels are commercially available. The TomICam technique therefore has significant advantages over other state-of-the-art high-resolution 3-D imaging modalities.

### 5.1.2 Tomographic Imaging Camera

In its basic implementation, the TomICam acquires an entire 2-D ( $x, y$ ) tomographic slice at a fixed depth  $z$ , as shown in figure 5.2b. A full 3-D image is obtained by a set of measurements where the axial ( $z$ ) location of the 2-D slice is tuned electronically.

An intuitive description of the TomICam principle is shown in figure 5.3. The conventional FMCW measurement in figure 5.3a produces peaks in the photocurrent

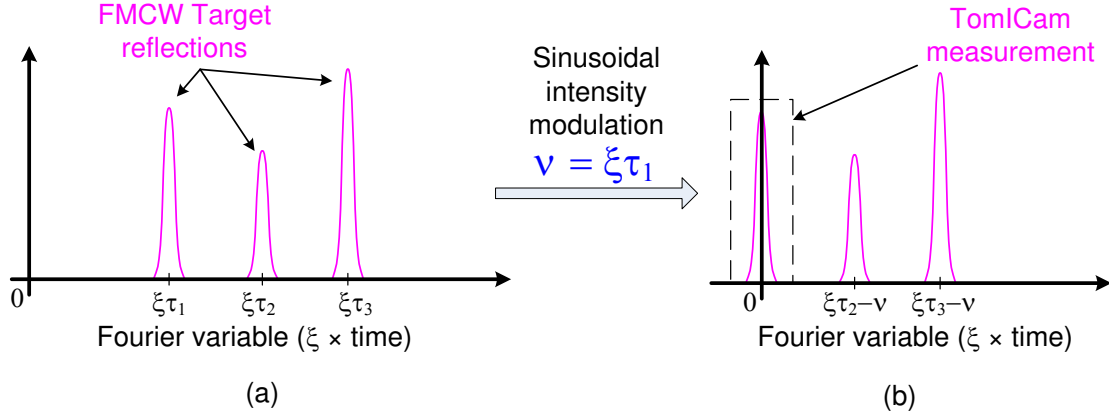


Figure 5.3: (a) Spectrum of the FMCW photocurrent. The peaks at frequencies  $\xi\tau_1$ ,  $\xi\tau_2$ , and  $\xi\tau_3$ , where  $\xi$  is the chirp rate, correspond to scatterers at  $\tau_1$ ,  $\tau_2$ , and  $\tau_3$ . (b) The beam intensity is modulated with a frequency  $\xi\tau_1$ , shifting the signal spectrum, such that the peak due to a reflector at  $\tau_1$  is now at DC. This DC component is measured by a slow integrating detector.

spectrum, each peak corresponding to a scatterer at a particular depth ( $z$ ) within the sample. If a sinusoidal modulation is imposed on the optical intensity, and hence on the photocurrent, the spectrum is shifted towards DC. In figure 5.3b, the DC component of the shifted spectrum is measured by a slow detector (e.g., a pixel in a CCD or CMOS array). The entire spectrum is recovered by changing the modulation frequency over several scans. This scheme supplants the need for computing the Fourier transform and thus effects a reduction in system complexity. Inherent compatibility with compressive sensing further reduces the number of measurements necessary to reconstruct the full 3-D scene.

In the following sections we develop the formalism necessary to describe the TomICam principle and its extension with compressive sensing.

### 5.1.2.1 Summary of FMCW Reflectometry

A detailed description of the FMCW ranging system is presented in chapter 2. Here, we briefly summarize the FMCW analysis to set the scene for TomICam. Consider the FMCW experiment shown in figure 5.4a. We analyze the response of this system under excitation by an SFL with a linear frequency sweep,  $\omega(t) = \omega_0 + \xi t$ . We assume that the sample comprises a set of scatterers with reflectivities  $R_n$  and round-

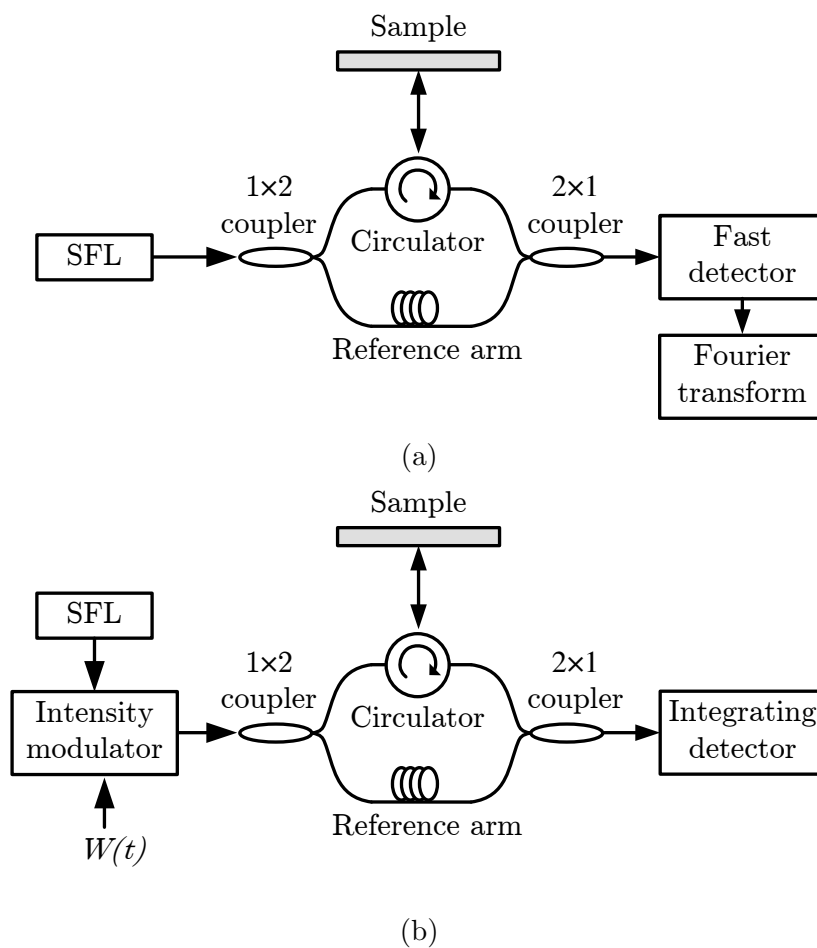


Figure 5.4: (a) Single-pixel FMCW system. The interferometric signal is recorded using a fast photodetector, and reflector information is recovered at all depths at once. (b) Single-pixel TomICam. The beam intensity is modulated with a sinusoid, and the interferometric signal is integrated using a slow detector. This gives one number per scan, which is used to calculate the reflector information at a particular depth, determined by the modulation frequency.

trip delays  $\tau_n$ ; and that these delays are smaller than the laser coherence time, so that any phase noise contribution can be neglected. The normalized photocurrent is equal to the time-averaged intensity of the incident beam (see chapter 2),

$$\begin{aligned} i_{\text{FMCW}}(t) &= \left\langle \left| e(t) + \sum_n \sqrt{R_n} e(t - \tau_n) \right|^2 \right\rangle \\ &= \text{rect} \left( \frac{t - T/2}{T} \right) \sum_n \sqrt{R_n} \cos \left[ (\xi \tau_n) t + \omega_0 \tau_n - \frac{\xi \tau_n^2}{2} \right], \end{aligned} \quad (5.1)$$

where  $T$  is the scan duration,  $\xi$  is the slope of the optical chirp,  $\phi_0$  and  $\omega_0$  are the initial phase and frequency, respectively, and only the cross terms were retained for simplicity. The total frequency excursion of the source (in Hz) is therefore given by  $B = \xi T / 2\pi$ . A Fourier transform of this photocurrent results in a map of scatterers along the direction of beam propagation (e.g., figure 5.3a). The strength of a scatterer at some delay  $\tau$  is given by the intensity of the Fourier transform of equation (5.1), evaluated at a frequency  $\nu = \xi\tau$ :

$$|Y(\nu = \xi\tau)|^2 = \left| \int_0^T \exp [j(\xi\tau)t] i_{\text{FMCW}}(t) dt \right|^2. \quad (5.2)$$

By the Fourier uncertainty relation, the resolution of this measurement is inversely proportional to the integration time  $T$ . The spatial resolution is, therefore, given by

$$\Delta z = \frac{c}{2} \frac{2\pi}{\xi} \frac{1}{T} = \frac{c}{2B}, \quad (5.3)$$

where  $c$  is the speed of light.<sup>1</sup>

### 5.1.2.2 TomICam Principle

The key idea behind TomICam is that the Fourier transform required for FMCW data processing may be performed in hardware using an integrating photodetector, e.g. a pixel in a CCD or CMOS imaging array. To this end, we modify the basic FMCW experiment to include an intensity modulator, as shown in figure 5.4b. The

---

<sup>1</sup>The scatterer range is given by  $z = c\tau/2$ .

integrating detector is reset at the beginning of every sweep, and sampled at the end. For a given modulation signal  $W(t)$ , the beat signal at the detector is given by

$$y_W(t) \propto W(t) i_{\text{FMCW}}(t). \quad (5.4)$$

The value sampled at the output of the integrating detector is therefore given by

$$Y_W = \int_0^T W(t) i_{\text{FMCW}}(t) dt, \quad (5.5)$$

where  $Y_W$  is the TomICam measurement corresponding to an intensity modulation waveform  $W(t)$ , and we assumed an overall system gain of 1 for simplicity. The TomICam measurement therefore amounts to projecting the FMCW photocurrent of equation (5.1) onto a basis function described by the modulation  $W(t)$ .

We consider two modulations:  $W_C = \cos [(\xi\tau)t]$ , and  $W_S = \sin [(\xi\tau)t]$ , which correspond to the cosine and sine transforms.

$$Y_{W_C}(\tau) = \int_0^T \cos [(\xi\tau)t] i_{\text{FMCW}}(t) dt \quad (5.6)$$

$$Y_{W_S}(\tau) = \int_0^T \sin [(\xi\tau)t] i_{\text{FMCW}}(t) dt \quad (5.7)$$

Equation (5.2) may therefore be written as:

$$|Y(\nu = \xi\tau)|^2 = |Y_{W_C}(\tau) + j * Y_{W_S}(\tau)|^2 = |Y_{W_C}(\tau)|^2 + |Y_{W_S}(\tau)|^2. \quad (5.8)$$

The scatterer strength at a delay  $\tau$  is calculated using two consecutive scans. The strength of the TomICam platform lies in its ability to generate depth scans using low-bandwidth integrating detectors, making possible the use of a detector array, such as a CMOS or CCD camera. A possible extension to a 2-D integrating detector array is shown in figure 5.5. Each element in the array performs a TomICam measurement at a particular lateral  $(x, y)$  location, as described above. The TomICam platform

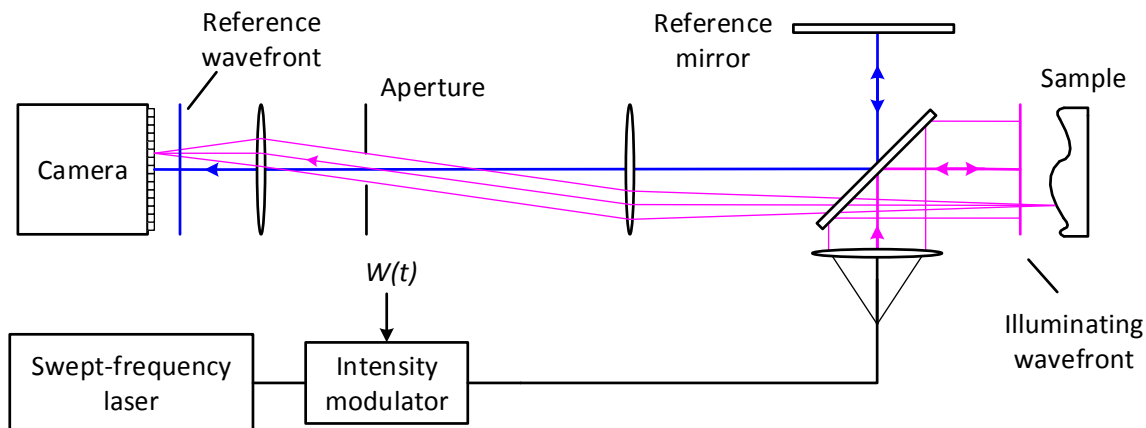


Figure 5.5: A possible TomICam configuration utilizing a CCD or CMOS pixel array in a Michelson interferometer. Each transverse point  $(x, y)$  at a fixed depth  $(z)$  in the object space is mapped to a pixel on the camera. The depth  $(z)$  is tuned electronically by adjusting the frequency of the modulation waveform  $W(t)$ .

therefore has the following important features:

- A full tomographic slice is obtained in a time that is only limited by the chirp duration. This is orders of magnitude faster than a raster-scanning solution, and enables real-time imaging of moving targets.
- The depth of the tomographic slice is controlled by the electronic waveform  $W(t)$ , so that the entire 3-D sample space can be captured without moving parts.
- It leverages the integrating characteristic of widely available inexpensive CCD and CMOS imaging arrays to substantially reduce signal processing overhead.
- It is scalable to a large number of transverse pixels with no increase in acquisition or processing time.
- The TomICam platform is not limited to sinusoidal modulations  $W(t)$ , making it inherently suitable for compressive sensing, as described in section 5.2.

### 5.1.2.3 TomICam Proof-of-Principle Experiment

In order to verify the equivalence of FMCW and TomICam measurements, we have performed a proof-of-principle experiment, shown schematically in figure 5.6. We

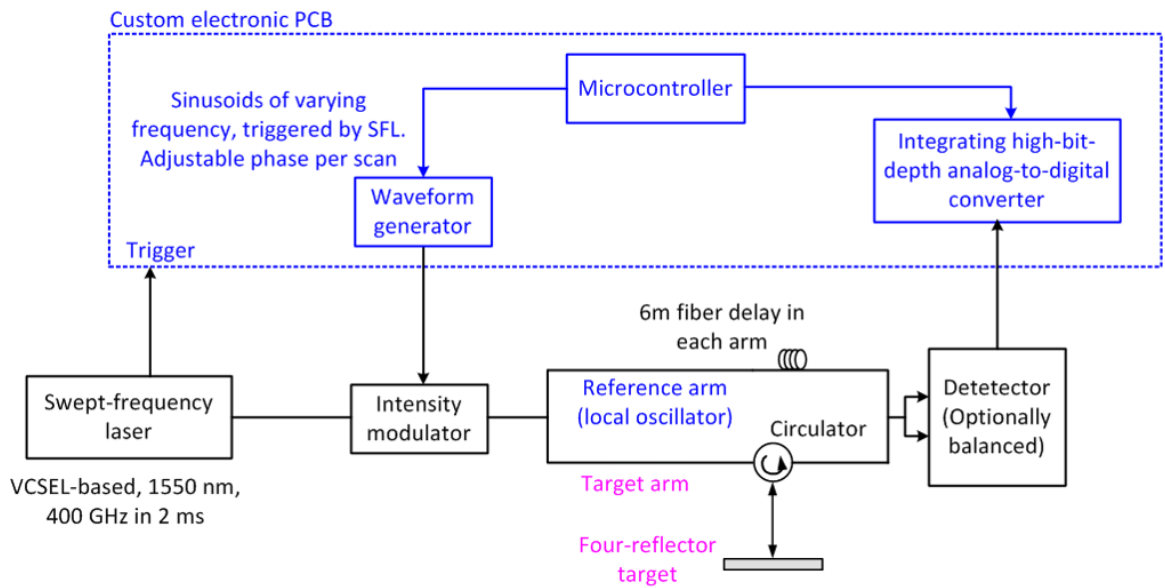


Figure 5.6: Schematic diagram of the TomICam proof-of-principle experiment. A slow detector was modeled by a fast detector followed by an integrating analog-to-digital converter. The detector signal was sampled in parallel by a fast oscilloscope, to provide a baseline FMCW depth measurement.

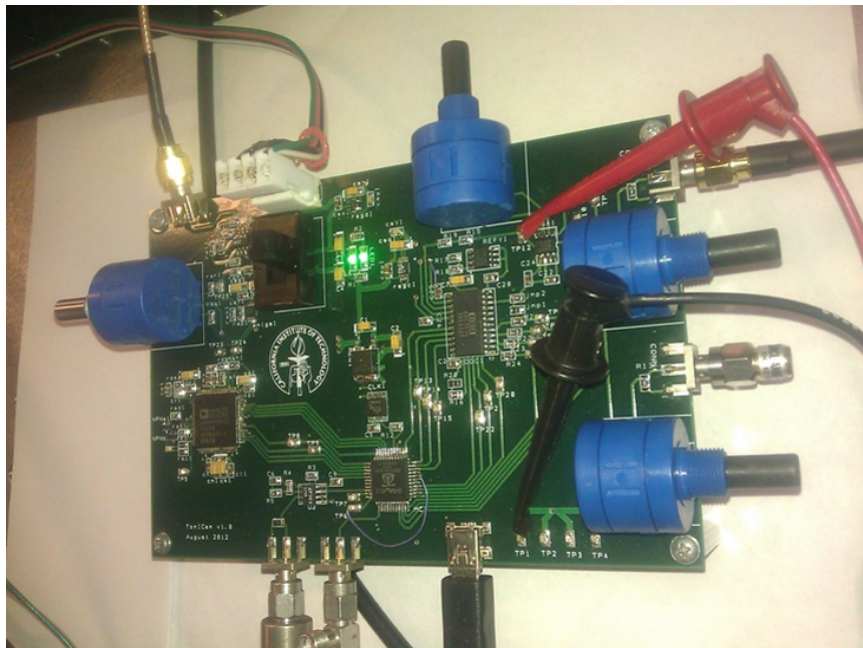


Figure 5.7: The custom PCB used in the TomICam experiment. Implemented functionality includes triggered arbitrary waveform generation and high-bit-depth acquisition of an analog signal.

used the 1550 nm VCSEL-based optoelectronic SFL, described in section 3.4.1, which produced a precisely linear chirp with a swept optical bandwidth of 400 GHz, and a scan time of 2 ms. The beam was modulated using a commercially available lithium niobate intensity modulator.

The necessary electronic functionality, including an arbitrary waveform generator, an integrating high-bit-depth analog-to-digital converter, and a microcontroller, was implemented on a PCB, shown in figure 5.7. The waveform generator was used to provide sine and cosine waveforms of different frequencies to the intensity modulator. The amplitude of these waveforms was apodized by a Hamming window, which suppressed the sinc sidebands associated with a rectangular apodization. The integrating analog-to-digital converter recorded a single number per scan. The microcontroller was used to coordinate the waveform generation and signal acquisition. The photodetector output was also sampled on a high-speed oscilloscope in order to provide a baseline FMCW measurement.

We used a sample comprising two acrylic slabs. Reflections from the air-acrylic and acrylic-air interfaces were recorded and the results are shown in figure 5.8. The red curve is the intensity of the Fourier transform of the FMCW photocurrent. The blue curve is constructed by varying the frequencies of the modulation waveforms  $W_C(t)$  and  $W_S(t)$ , and applying equation (5.8). As expected, the two curves are practically identical.

We note that a copy of the signal, scaled in frequency by a factor of  $\frac{1}{3}$ , shows up in the TomICam spectrum in figure 5.8. This ghost replica is due to a third-order nonlinearity exhibited by our intensity modulator, and can be resolved through the use of a linear intensity modulator. An example of such a modulator is the amplitude controller based on a semiconductor optical amplifier in a feedback loop, described in section 3.3.2.

We characterize the dynamic range of our system by performing FMCW and TomICam measurements on a fiber Mach-Zehnder interferometer (MZI). We introduce optical attenuation in one of the MZI arms, and measure the signal SNR. The results for unbalanced and balanced acquisition in FMCW and TomICam configura-

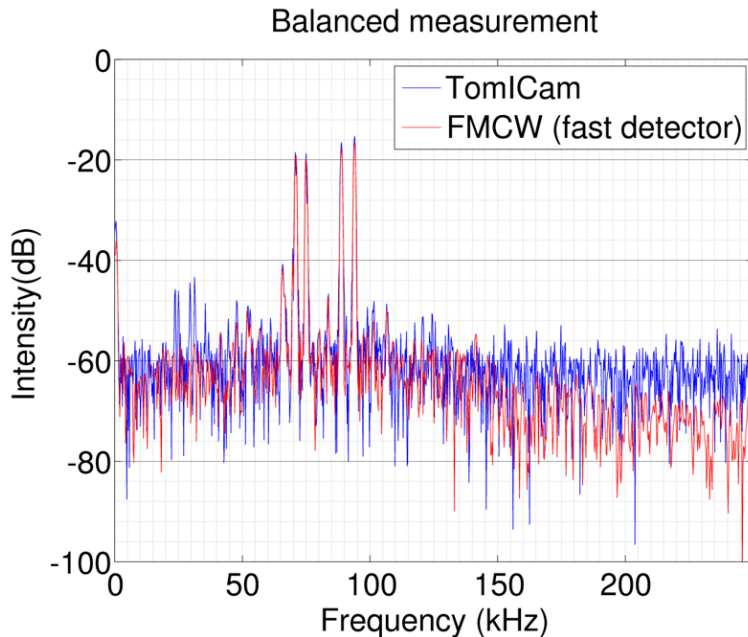


Figure 5.8: Comparison between FMCW (red) and TomICam (blue) depth measurements. The two are essentially identical except for a set of ghost targets at  $\frac{1}{3}$  of the frequency present in the TomICam spectrum. These ghosts are due to the third-order nonlinearity of the intensity modulator used in this experiment.

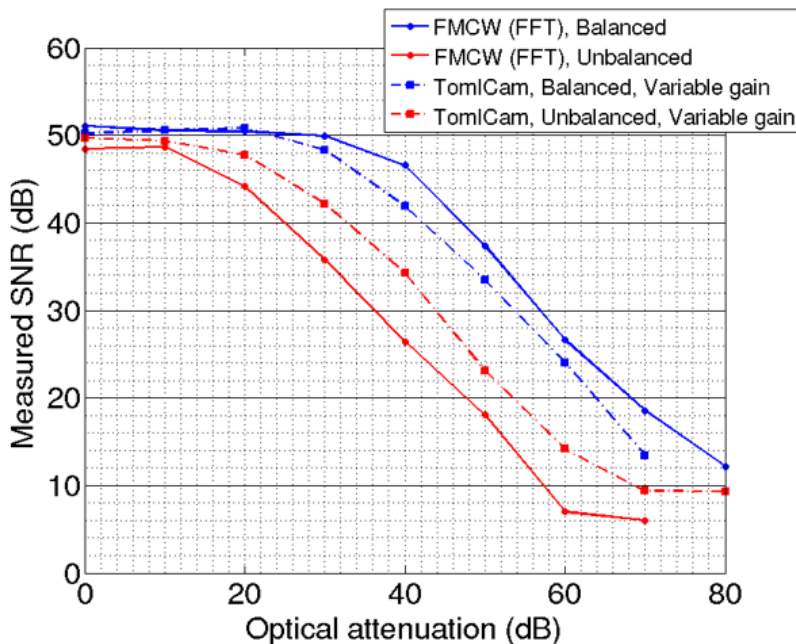


Figure 5.9: Characterization of the FMCW and TomICam dynamic range. The signal-to-noise ratio was recorded as a function of attenuation in one of the interferometer arms. At low attenuations, the SNR saturates due to SFL phase noise and residual nonlinearity.

tions are shown in figure 5.9. The dynamic range of our system, defined as the ratio of the strongest to weakest measurable target reflectivity, is about  $\sim 80$  dB. For low attenuation, i.e., large reflectivities, the SNR is limited by the laser coherence and residual chirp nonlinearity, saturating at a (path-length mismatch dependent) value of  $\sim 50$  dB. The fiber mismatch used in this experiment was about 40 mm.

## 5.2 Compressive Sensing

The total number of tomographic slices,  $N$ , used in a 3-D image reconstruction is given by the axial extent,  $L_z$ , of the target divided by the axial resolution,  $\Delta z$ . We note that most real life targets are sparse in the sense that they have a limited number of scatterers,  $k$ , in the axial direction. The acquisition of  $N \gg k$  slices to form the 3-D image is therefore inefficient. In this section, we investigate the use of compressive sensing (CS) in conjunction with the TomICam platform in order to obtain the 3-D image with many fewer than  $N$  measurements. This has the potential to reduce the image acquisition time and the optical energy requirement of the TomICam by orders of magnitude.

### 5.2.1 Compressive Sensing Background

We briefly state the salient features of CS [69]. Consider a linear measurement system of the form:

$$\mathbf{y} = \mathbf{A}\mathbf{x} \quad \mathbf{A} \in \mathbb{C}^{m \times N}, \mathbf{x} \in \mathbb{C}^N, \mathbf{y} \in \mathbb{C}^m, \quad (5.9)$$

where the vector  $\mathbf{x}$  is the signal of interest, and the vector  $\mathbf{y}$  represents the collected measurements. The two are related by the measurement matrix  $\mathbf{A}$ . The case of interest is the highly under-determined case,  $m \ll N$ . The system therefore possesses infinitely many solutions. Nevertheless, CS provides a framework to uniquely recover  $\mathbf{x}$ , given that  $\mathbf{x}$  is sufficiently sparse, and the measurement matrix  $\mathbf{A}$  satisfies certain properties such as restricted isometry and incoherence [69]. The intuition behind CS

is to perform the measurements in a carefully chosen basis where the representation of the signal  $\mathbf{x}$  is not sparse. The signal is then recovered by finding the sparsest  $\mathbf{x}$  that is consistent with the measurement in equation (5.9). Specifically, the recovery is accomplished by solving a convex minimization problem:

$$\begin{aligned} & \text{minimize} && \|\mathbf{x}\|_1 \\ & \text{subject to} && \mathbf{A}\mathbf{x} = \mathbf{y}, \end{aligned} \tag{5.10}$$

where  $\|\mathbf{x}\|_1$  denotes the  $l_1$  norm of  $\mathbf{x}$ . The use of the  $l_1$  norm promotes sparse solutions, while maintaining convexity of the minimization problem, resulting in a tractable computation time. Success of recovery depends on the number of measurements  $m$ , the sparsity level of  $\mathbf{x}$ , and the properties of the measurement matrix  $\mathbf{A}$ . This approach is of particular interest due to continuous advances in computational algorithms that improve the reconstruction speed [72].

### 5.2.2 TomICam Posed as a CS Problem

Fundamentally, the FMCW imaging technique converts the reflection from a given depth in the  $z$  direction to a sinusoidal variation of the detected photocurrent at a frequency that is proportional to the depth. Scatterers from different depths thus result in a photocurrent with multiple frequency components. In its basic implementation (section 5.1.2.2), the TomICam uses a single-frequency modulation of the beam intensity to determine one of these possible frequency components. Full image acquisition requires  $N$  measurements ( $N = L_z/\Delta z$ ), determined by the axial resolution of the swept-frequency source. When the number of axial scatterers—and hence the number of frequency components in the photocurrent—is sparse, the CS framework enables image acquisition with a smaller number of measurements.

We first show that the TomICam is inherently suited to compressive imaging and that different types of measurements may be easily performed with almost no modification to the system. We recast equation (5.5) in a form more suitable for the discussion of CS. We assume that there are  $N$  possible target locations with

corresponding delays  $\tau_n$ ,  $n = 0, 1, \dots, (N - 1)$  and target reflectivities  $R_n$ . These target locations are separated by the axial resolution:  $\tau_n = n/B$ . We assume that the target is  $k$ -sparse so that only  $k$  of the  $N$  possible reflectivities are nonzero. The time axis is discretized to  $N$  points given by  $t_h = \frac{hT}{N}$ ,  $h = 0, 1, \dots, (N - 1)$ . Equation (5.5) can now be written as

$$y = \sum_{h=0}^{N-1} \sum_{n=0}^{N-1} W(t_h) \frac{\sqrt{R_n}}{N} \cos(\xi\tau_n t_h + \omega_0\tau_n). \quad (5.11)$$

Each TomICam measurement therefore yields a single value  $y$  for a particular  $W(t_h)$  (per pixel in the lateral plane), as given by equation (5.11). Note that a sinusoidal variation of  $W(t_h)$  yields the reflectivity at a particular axial depth, and a tomographic slice is obtained using a detector array, as described in section 5.1.2.2.

In this section, we will explore other intensity modulation waveforms  $W(t_h)$  that are compatible with the CS framework to reduce the number of scans in the axial dimension. We extend the discussion to include  $m$  measurements indexed by  $s$ , i.e., we will use  $m$  different intensity modulation waveforms  $W_s(t_h)$  to obtain  $m$  distinct measurements  $y_s$ . Equation (5.11) can be simplified to give

$$\begin{aligned} y_s &= \sum_{h=0}^{N-1} \sum_{n=0}^{N-1} W_s\left(\frac{hT}{N}\right) \cdot \frac{1}{\sqrt{N}} \exp\left(-j\frac{2\pi hn}{N}\right) \cdot \sqrt{\frac{R_n}{N}} \exp\left(-j\frac{\omega_0}{B}n\right) \\ &= \sum_{h=0}^{N-1} \sum_{n=0}^{N-1} W_{sh} \cdot F_{hn} \cdot x_n, \end{aligned} \quad (5.12)$$

where  $W_{sh} \equiv W_s\left(\frac{hT}{N}\right)$ ,  $F_{hn} \equiv \frac{1}{\sqrt{N}} \exp\left(-j\frac{2\pi hn}{N}\right)$ ,  $x_n \equiv \sqrt{\frac{R_n}{N}} \exp\left(-j\frac{\omega_0}{B}n\right)$ , and it is understood that the measurements correspond to the real part of the right hand side. Rewriting equation (5.12) in matrix notation, we obtain:

$$\mathbf{y} = \mathbf{W}\mathbf{F}\mathbf{x}, \quad (5.13)$$

where  $\mathbf{x}$  is the  $k$ -sparse target vector of length  $N$ ,  $\mathbf{y}$  is the vector containing the  $m$  TomICam measurements,  $\mathbf{F}$  is the  $N \times N$  unitary Fourier matrix, and  $\mathbf{W}$  is the  $m \times N$

matrix that comprises the  $m$  intensity modulation waveforms  $W_s(t_h)$ .

Since  $\mathbf{W}$  is electrically controlled, a variety of measurement matrices can therefore be programmed in a straightforward manner. Each TomICam measurement  $y_s$  is obtained by multiplying the optical beat signal with a unique modulation waveform  $W_s(t_h)$  and integrating over the measurement interval. If the modulation waveforms are chosen appropriately, the measurement matrix can be made to satisfy the crucial requirements for CS, i.e., the restricted isometry property and incoherence [69]. This ensures that the information about the target—which is sparse in the axial dimension—is “spread out” in the domain in which the measurement is performed, and a much smaller number of measurements is therefore sufficient to successfully recover the complete image.

### 5.2.3 Robust Recovery Guarantees

We now consider two possibilities for  $\mathbf{W}$  that yield a measurement matrix capable of robust signal recovery. These represent straightforward implementations of CS TomICam imaging.

#### 5.2.3.1 Random Partial Fourier Measurement Matrix

A random partial Fourier matrix of size  $m \times N$  is generated by selecting  $m$  rows at random from the  $N \times N$  Fourier matrix  $\mathbf{F}$ . This operation is accomplished by a binary matrix  $\mathbf{W}$  that has a single nonzero entry in each row. The location of the nonzero entry is chosen randomly without replacement. For this class of matrices, robust signal recovery is guaranteed whenever the number of measurements satisfies [73]

$$m \geq Ck \log(N/\epsilon), \quad (5.14)$$

where  $k$  is the signal sparsity,  $1 - \epsilon$  is the probability of recovery, and  $C$  is a constant of order unity.

In the TomICam implementation, a random partial Fourier measurement corresponds to pulsing the intensity modulator during the linear chirp, so that only a single

optical frequency is delivered to the target per scan, leaving a lot of dead time. As a result, the optoelectronic SFL is not the most ideal laser candidate, and other sources that can provide rapid random frequency access, such as sampled grating SCLs, are more suitable [74]. In these devices, the cavity mirrors are formed using a pair of sampled gratings, each of which has multiple spectral reflection bands. Current tuning of the mirror sections is used to make these reflection bands overlap, forming a single band whose position may be varied over a broad spectral range. Further, a phase section current is applied to align a Fabry-Pérot cavity mode to the middle of the band in order to optimize lasing properties. Simultaneously tuning all three sections enables broadband frequency access, approaching 5 THz at 1550 nm [75].

### 5.2.3.2 Gaussian or Sub-Gaussian Random Measurement Matrix

This class of matrix has the property that any entry  $A_{ij}$  in the matrix  $\mathbf{A}$  is randomly chosen from independent and identical Gaussian or sub-Gaussian distributions. In this case, robust signal recovery is guaranteed for

$$m \geq Ck \log(N/k), \quad (5.15)$$

where  $k$  is the signal sparsity, and  $C$  is a constant of order unity. Moreover, the same result also applies to a measurement matrix that is a product of a Gaussian or sub-Gaussian random matrix and a unitary matrix. Since  $\mathbf{F}$  is unitary, a Gaussian random matrix  $\mathbf{W}$  results in robust signal recovery when equation (5.15) is satisfied [76]. The measurements obtained using a Gaussian matrix  $\mathbf{W}$  may be interpreted as a collection of conventional TomICam measurements where each measurement queries all possible depths with different weights.

We want the failure rate  $\epsilon$  to be much less than unity, while the sparsity level  $k$  is at least unity. Therefore, the Gaussian random matrix requires fewer measurements than the random partial Fourier matrix for correct recovery.

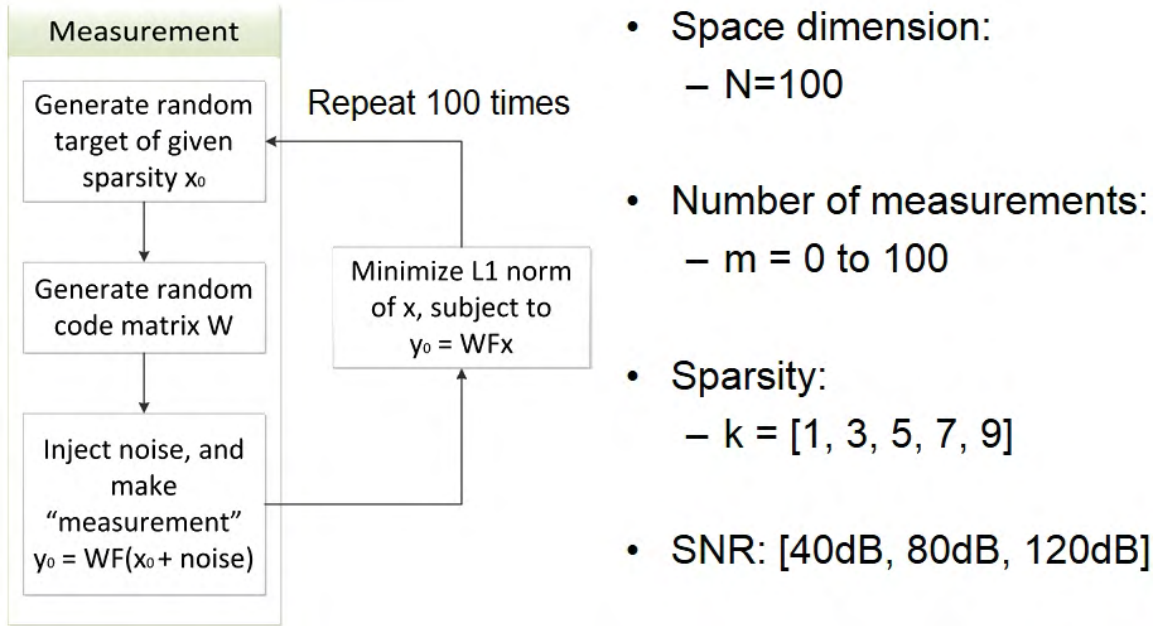


Figure 5.10: Flow diagram and parameters of the CS TomICam simulation

#### 5.2.4 Numerical CS TomICam Investigation

Because the partial Fourier matrix is not well-suited for the TomICam platform, we continue our investigation with the Gaussian random matrix in mind. We evaluate the performance of a compressively-sampled TomICam through a series of numerical simulations. The simulation steps and parameters are summarized in figure 5.10.

We consider a signal space with dimension  $N = 100$ , and generate a random target signal  $\mathbf{x}_0$  of a given sparsity. We generate a Gaussian random matrix  $W$  of size  $m \times N$ , where  $m$  is the number of measurements. We then make a noisy measurement

$$\mathbf{y}_0 = \mathbf{W}\mathbf{F}(\mathbf{x}_0 + \mathbf{x}_n), \quad (5.16)$$

where  $\mathbf{x}_n$  is a randomly generated noise vector. We define the SNR as the ratio of the signal and noise energies,

$$\text{SNR} \equiv \frac{\|\mathbf{x}_0\|_2}{\|\mathbf{x}_n\|_2}. \quad (5.17)$$

We then proceed to solve the convex minimization problem in equation (5.10), which yields the recovered signal  $\mathbf{x}$ . We define the signal-to-error ratio (SER) as the ratio of

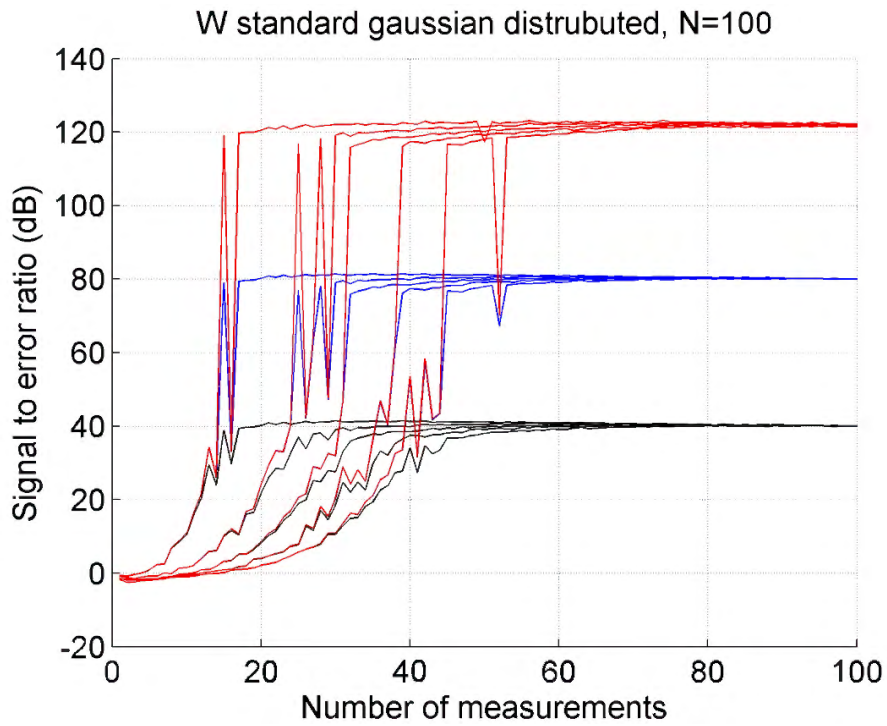


Figure 5.11: SER curves for a CS simulation with a Gaussian random matrix

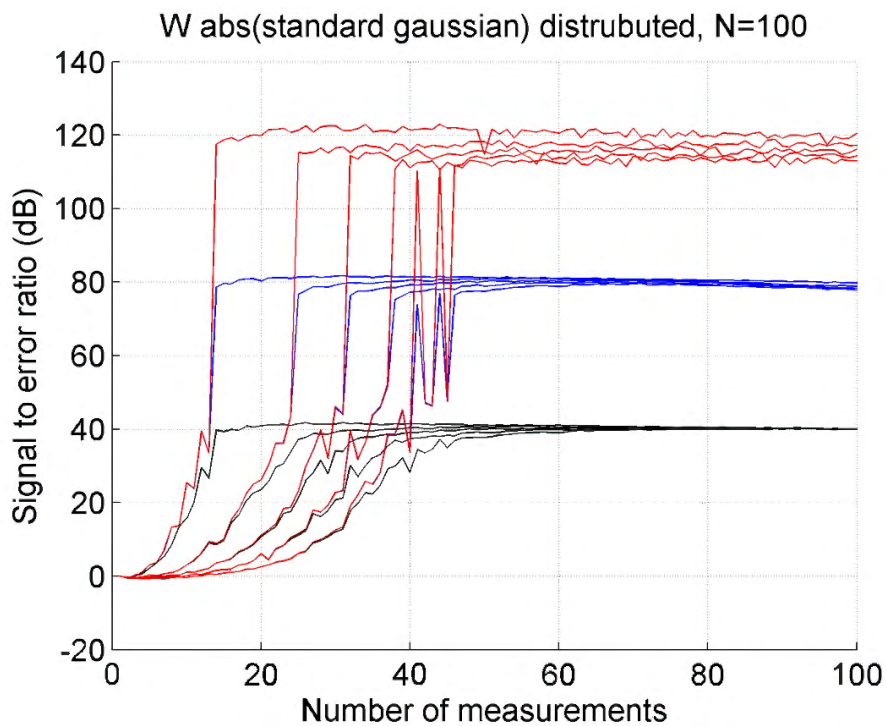


Figure 5.12: SER curves for a CS simulation with a waveform matrix given by the absolute value of a Gaussian random matrix

the energy of the recovered signal to the energy of the difference between the recovered and the original signals.

$$\text{SER} \equiv \frac{\|\mathbf{x}\|_2}{\|\mathbf{x} - \mathbf{x}_0\|_2}. \quad (5.18)$$

We repeat this procedure 100 times and record the average SER. We consider  $0 < m < 100$ , and simulate 100 reconstructions for each value of  $m$ , resulting in a curve of SER vs.  $m$ . We generate 15 such a curves by considering five sparsity levels  $k = [1, 3, 5, 7, 9]$ , and three noise levels  $\text{SNR} = [40\text{dB}, 80\text{dB}, 120\text{dB}]$ .

These curves are plotted in figure 5.11, with the 120 dB SNR shown in red, 80 dB in blue, and 40 dB in black. We expect that for a small number of measurements, the reconstructions will fail, yielding a zero SER. Once the number of measurements satisfies equation (5.15), the reconstruction will essentially always succeed, yielding an SER that is approximately equal to the SNR. This is the pattern that we see in figure 5.11. The curves corresponding to the different sparsity levels are in order, with the sparsest case achieving the transition in SER at the lowest number of measurements. We observe that  $\sim 50$  measurements are necessary to recover a 9-sparse target, which corresponds to a factor of two compression, when compared to conventional sampling.

We note that a Gaussian random matrix has negative entries, and is therefore not physical (we can only modulate the beam intensity with a positive waveform). To fix this, we investigate numerically random matrices that contain only positive entries. SER curves for  $\mathbf{W}$  given by the absolute value of a Gaussian random matrix are shown in figure 5.12. The qualitative behavior of the curves is unchanged from the random Gaussian case.

A passive intensity modulator can only provide a modulation between 0 and 1, and we therefore examine a waveform matrix  $\mathbf{W}$  with entries that are uniformly distributed between 0 and 1. The SER curves for this case are shown in figure 5.13, and follow the trend of the previous simulations.

Realistic intensity modulators have a finite extinction ratio, meaning they cannot be used to turn the beam completely off. Moreover, it may be desirable to operate the

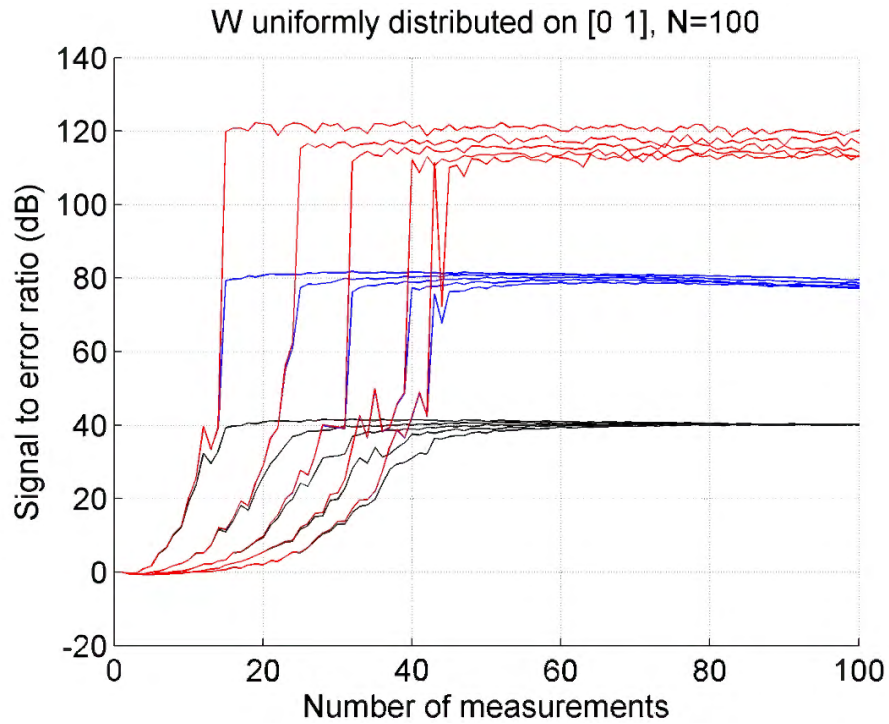


Figure 5.13: SER curves for a CS simulation with a waveform matrix whose entries are uniformly distributed between 0 and 1

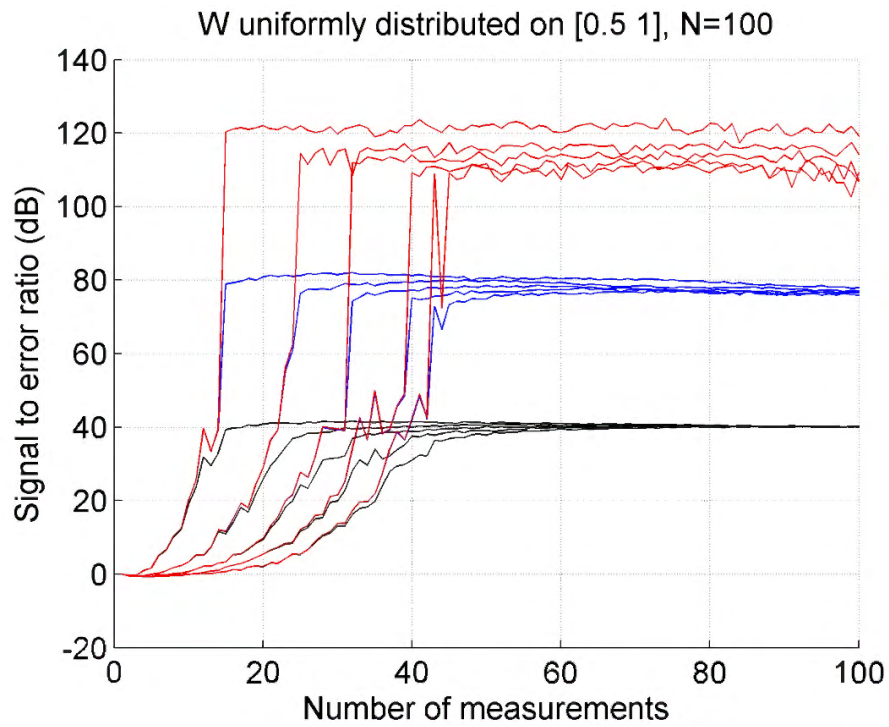


Figure 5.14: SER curves for a CS simulation with a waveform matrix whose entries are uniformly distributed between 0.5 and 1

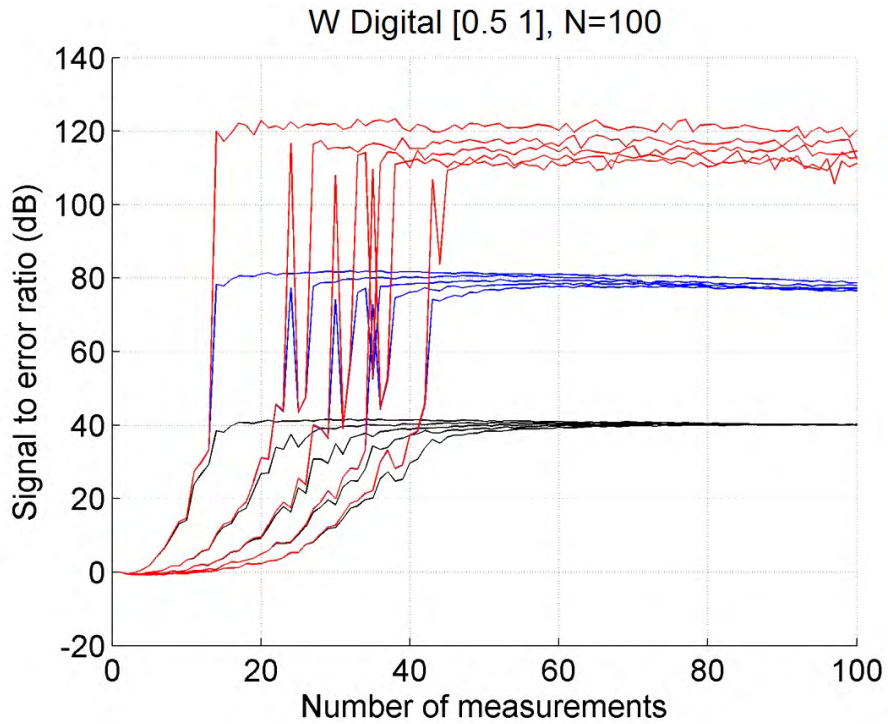


Figure 5.15: SER curves for a CS simulation with a waveform matrix whose entries take on the values of 0.5 or 1 with equal probabilities

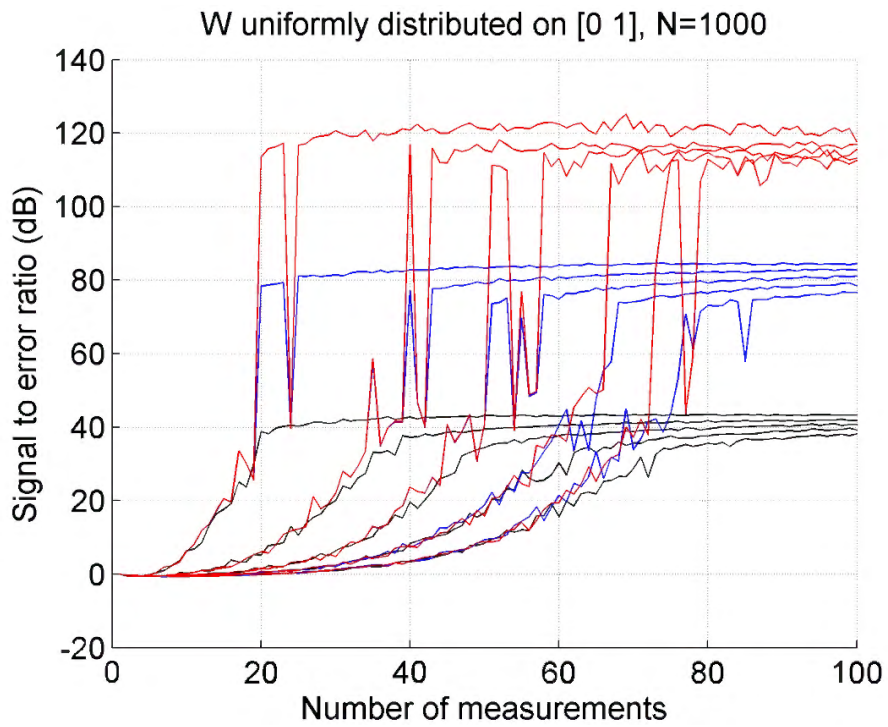


Figure 5.16: SER curves for an  $N = 1000$  CS simulation with a waveform matrix whose entries are uniformly distributed between 0.5 and 1

intensity modulator away from the zero point to keep its response as linear as possible. To account for this possibility we ran the simulation using a waveform matrix  $\mathbf{W}$  with entries that are uniformly distributed between 0.5 and 1. Again, the transition trends for the SER curves, shown in figure 5.14 remain essentially unchanged.

The waveform generator has a finite bit depth, and we consider, as an extreme case, only two modulation levels—0.5 and 1—which corresponds to a waveform matrix  $\mathbf{W}$  whose entries can equal either of the modulation levels with equal probabilities. The SER curves for this simulation are shown in figure 5.15, and again demonstrate the same behavior.

For our final simulation we increased the dimension of the space to 1000, and used a waveform matrix  $\mathbf{W}$  with entries that are uniformly distributed between 0 and 1. The SER curves for this simulation are shown in figure 5.16. We observe that  $\sim 80$  measurements are necessary to recover a 9-sparse target, which corresponds to greater than  $10\times$  compression, when compared to conventional sampling.

### 5.3 Summary

In this chapter we described the basic tomographic imaging camera principle, and demonstrated single-pixel TomICam ranging in a proof-of-concept experiment. The TomICam uses a combination of electronically tuned optical sources and low-cost full-field detector arrays, completely eliminating the need for moving parts traditionally employed in 3-D imaging. This new imaging modality could be useful in a variety of established and emerging disciplines, including lidar [18], profilometry [22], biometrics [25], biomedical diagnostics [21, 26], 3-D manufacturing [27], and tissue engineering [28–31].

We also discussed the application of compressive sensing to the TomICam platform, and performed a series of numerical simulations. These simulations show that a factor of 10 reduction in the number of measurements is possible with CS if the number of depth bins is about 1000. Future implementations of TomICam will benefit from the development of high frame rate, high pixel count silicon CCD and CMOS

cameras, rapidly-tunable semiconductor lasers [77], efficient compressive sensing algorithms, and continuous advances in computing performance. As a result, TomICam has the potential to push 3-D imaging functionality well beyond the state of the art.